Investigating ultra-low velocity zones in the southern hemisphere using an Antarctic dataset

Samantha E. Hansen [a,*], Sarah E. Carson [a], Edward J. Garnero [b], Sebastian Rost [c], Shule Yu [b]

[a] *Department of Geological Sciences, The University of Alabama, United States of America*
[b] *School of Earth and Space Exploration, Arizona State University, United States of America*
[c] *School of Earth and Environment, University of Leeds, United Kingdom of Great Britain and Northern Ireland*

ARTICLE INFO

ABSTRACT

Given limited seismic coverage of the lowermost mantle, less than one-fifth of the core-mantle boundary (CMB) has been surveyed for the presence of ultra-low velocity zones (ULVZs). Investigations that sample the CMB with new geometries are therefore important to further our understanding of ULVZ origins and their potential connection to other deep Earth processes. Using core-reflected ScP waves recorded by the recently deployed Transantarctic Mountains Northern Network in Antarctica, the current study aims to expand ULVZ investigations in the southern hemisphere. Our dataset samples the CMB in the vicinity of New Zealand, providing coverage between an area to the northeast, where ULVZ structure has been previously identified, and another region to the south, where prior evidence for a ULVZ was inconclusive. This area is of particular interest because the data sample across the boundary of the Pacific Large Low Shear Velocity Province (LLSVP). The Weddell Sea region near Antarctica is also well sampled, providing new information on a region that has not been previously studied. A correlative scheme between a large database of 1-D synthetic seismograms and the observed ScP data demonstrates that ULVZs are required in both study regions. Modeling uncertainties limit our ability to definitively define ULVZ characteristics but also likely indicate more complex 3-D structure. Given that ULVZs are detected within, along the edge of, and far from the Pacific LLSVP, our results support the hypothesis that ULVZs are compositionally distinct from the surrounding mantle and are not solely related to partial melt. ULVZs may be ubiquitous along the CMB; however, they may be thinner in many regions than can be resolved by current methods. Mantle convection currents may sweep the ULVZs into thicker piles in some areas, pushing these anomalies toward the boundaries of LLSVPs.

© 2020 The Author(s). Published by Elsevier B.V. This is an open access article under the CC BY-NC-ND license (http://creativecommons.org/licenses/by-nc-nd/4.0/).

1. Introduction

The solid silicate mantle and the liquid iron-nickel outer core meet at the core-mantle boundary (CMB), which represents the largest absolute density contrast on our planet. Many investigations have documented thermal and compositional heterogeneities along the mantle-side of this boundary, with seismological studies providing the most detailed information, especially at small scales (*e.g.*, Hernlund and McNamara, 2015).

Along some portions of the CMB, structural heterogeneities identified as ultra-low velocity zones (ULVZs) have been detected. These laterally-varying structures have thicknesses on the order of tens of kilometers and are generally associated with reduced seismic wave velocities and increased density. However, ULVZ proper-

ties vary amongst different studies (see review by Yu and Garnero, 2018), making determination of the source of these anomalous structures challenging. Only ~17% of the CMB has been surveyed for the presence of ULVZs (*e.g.*, Yu and Garnero, 2018); thus, investigations with new CMB sampling geometries are desired to further constrain ULVZ origins.

The current study investigates ULVZ structure along previously unmapped sections of the CMB using core-reflections recorded by the Transantarctic Mountains Northern Network (TAMNNET), a 15-station seismic array that was recently deployed in Antarctica (Fig. 1A; Hansen et al., 2015). Given the locations of these stations and an abundance of deep, large magnitude earthquakes from areas around the Pacific, this study focuses on expanding ULVZ investigations in the southern hemisphere. More specifically, the TAMNNET data well sample the CMB adjacent to New Zealand, where previous studies have detected ULVZ structure to the northeast, but not the northwest, and inconclusive evidence was found
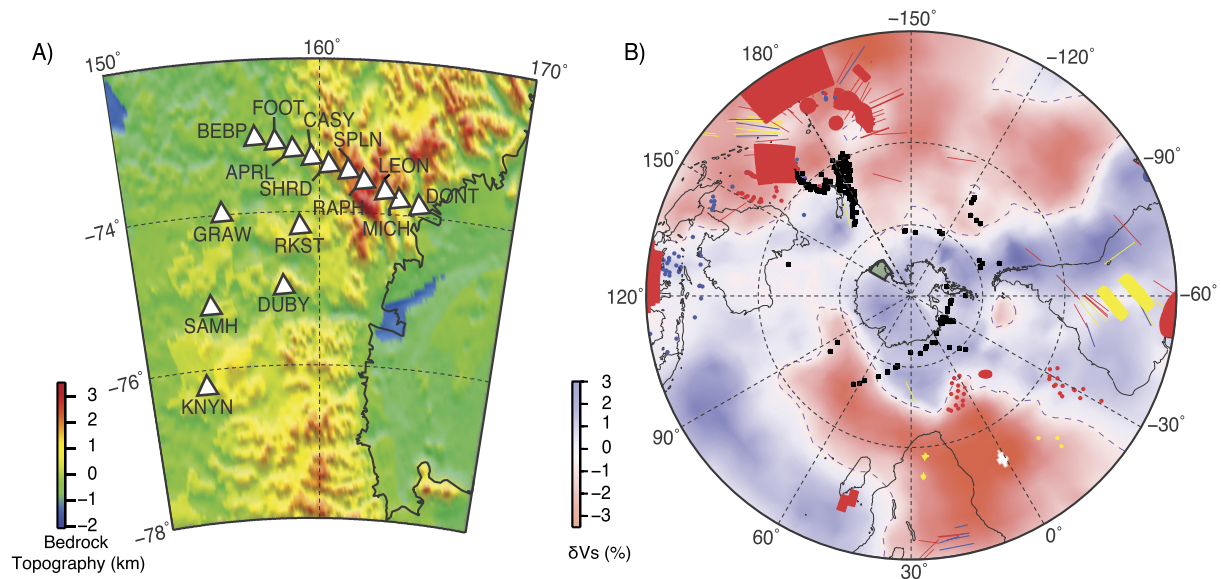
Fig. 1. Map of TAMNNET stations and previous ULVZ studies in the southern hemisphere. (A) TAMNNET stations (white triangles), overlain on bedrock topography from the BEDMAP2 model (Fretwell et al., 2013; note: sediment thickness not included). The location of this map is highlighted by the green polygon in (B). (B) Previous ULVZ studies, as summarized by Yu and Garnero (2018). Similar to Yu and Garnero (2018), red areas indicate regions where ULVZs have been detected, blue areas indicate regions where no ULVZ evidence has been found, and yellow areas indicate regions where ULVZ structure is uncertain. Additionally, black squares denote average ScP CMB bounce points locations for events examined in the current study. The GyPSuM tomography model (Simmons et al., 2010) at 2800 km depth is shown in the background, with purple dashed lines highlighting the LLSVP boundaries. Again, the green polygon highlights the location of the map shown in (A).
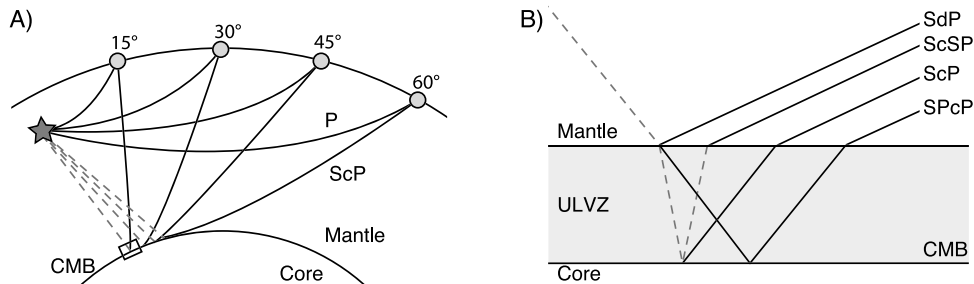
Fig. 2. Ray path diagram and ScP pre- and post-cursors. (A) Paths of direct P-waves and core-reflected ScP waves are shown at various distances. The earthquake at 500 km depth is shown as a star, S-waves are shown as dashed gray lines, and P-waves are shown as black lines. The black box highlights the region where ULVZ interaction may occur. (B) ScP pre- and post-cursors resulting from the interaction with a ULVZ. Black and dashed gray lines denote P- and S-waves, respectively. Modified from Brown et al. (2015).

to the south (Thorne and Garnero, 2004; Idehara et al., 2007; Pachhai et al., 2015). The current study fills the gap between these previously examined areas. Additionally, the New Zealand study area coincides with the edge of the Pacific Large Low Shear Velocity Province (LLSVP); therefore, the possible relationship between ULVZs and LLSVPs can be examined (e.g., Li et al., 2017; Yu and Garnero, 2018). The TAMNNET data also provide coverage of a portion of the CMB beneath the Weddell Sea, which is located far from any LLSVP and where no prior ULVZ studies have been conducted. By identifying and modeling core-reflected ScP waveforms from TAMNNET, we provide evidence for ULVZs in both study areas, thereby contributing important information to CMB structural investigations and the possible source of ULVZs.

2. Background and previous studies

2.1. Exploring CMB structure

A variety of seismic phases have been used to investigate ULVZs. Some investigations have focused on diffracted seismic waves (S_{diff}, P_{diff}; e.g., Xu and Koper, 2009; Cottaar and Romanowicz, 2012), including some phases that also pass through the outer core (PKP_{diff}, $PKKP_{diff}$, SP_dKS; e.g., Rondenay and Fischer, 2003; Frost

et al., 2013; Jensen et al., 2013). However, a challenge associated with employing some diffracted wave phases (e.g., SP_dKS) is the ambiguity of whether imaged ULVZ structure is present along the CMB at the source- or receiver-side of the wave path. There are also challenges with diffracted phases such as S_{diff} and P_{diff} due to long CMB sampling paths. Other studies instead utilize reflections from the CMB (ScP, PcP, ScS; e.g., Rost and Revenaugh, 2003; Avants et al., 2006; Brown et al., 2015). When a core-reflected wave interacts with a ULVZ, pre- and/or post-cursor arrivals may be generated (Garnero and Vidale, 1999). Pre-cursor energy arrives before the main core-reflected phase and can be associated with conversions or reflections from the top of the ULVZ, which can occur if the ULVZ is relatively flat (Yao and Wen, 2014; Brown et al., 2015). Post-cursor energy can arise from reverberations within the ULVZ layer and therefore appears as an arrival after the main core-reflected phase (Idehara et al., 2007). The current study focuses on ScP waves (Fig. 2). In the presence of a ULVZ, at least two ScP pre-cursors (SdP and SPcP) and one post-cursor (ScSP; Fig. 2) can be generated. Multiple reverberations in the ULVZ will arrive in the ScP coda, but they are typically too small in amplitude to be detected (Brown et al., 2015). The shape, timing, and amplitude of the pre- and post-cursors are strongly dependent on the thickness and shape of the ULVZ as well as its density and velocity

contrasts compared to the overlying mantle (*e.g.*, Garnero and Vidale, 1999; Reasoner and Revenaugh, 2000). Pre- and post-cursor arrivals are often small and therefore are more clearly visible when records are stacked. Further, by comparing the stacked ScP waveforms to stacked P waveforms, their differences can be studied to identify the pre- and post-cursor ULVZ energy (*e.g.*, Reasoner and Revenaugh, 2000; Rost and Revenaugh, 2003).

2.2. Characteristics, structure, and possible origins of ULVZs

ULVZs are small-scale laterally-varying structures characterized by density increases ($\delta\rho$) up to 20%, S-wave velocity reductions (δV_S) from $\sim$7-50%, and P-wave velocity reductions (δV_P) from $\sim$5-20%, with a few studies suggesting δV_P as high as 40% (see review by Yu and Garnero, 2018). While ULVZ thickness has been reported to vary from $\sim$2-100 km, thicknesses on the order of tens of kilometers are most common (*e.g.*, Yu and Garnero, 2018). ULVZs have also been estimated to be up to $\sim$900 km wide (Cottaar and Romanowicz, 2012; Thorne et al., 2013), but they are more commonly reported with smaller lateral extent (*e.g.*, 100-200 km). It is possible that many of the currently reported ULVZs are wider than indicated because thin, widespread ULVZs may fall below seismic resolution capabilities, which is typically $\sim$5-10 km (Rost et al., 2010), depending on the seismic probe. We also note that this minimum detection thickness is dependent upon other ULVZ properties.

Some investigations attribute ULVZs to thermal anomalies along the CMB, possibly associated with partial melt. Numerous studies (*e.g.*, Williams and Garnero, 1996; Garnero and Vidale, 1999; Reasoner and Revenaugh, 2000; Rost et al., 2006) have indicated an approximately 3:1 δV_S:δV_P ratio within ULVZs, consistent with 5-30% partial melt (dependent on melt geometries; *e.g.*, Williams and Garnero, 1996; Berryman, 2000). It has also been suggested that enhanced water content at the CMB could enable melting by lowering the eutectic point (Havens and Revenaugh, 2001) or that partial melt could accumulate along the CMB (Williams and Garnero, 1996). A number of studies have also correlated ULVZs with overlying hotspot locations, which may indicate that ULVZs feed mantle plumes (Williams et al., 1998; Garnero, 2000; Cottaar and Romanowicz, 2012).

However, some ULVZs have been identified outside presumably hot portions of the lower mantle, and not all ULVZs show the 3:1 δV_S:δV_P ratio associated with partial melt. In such cases, ULVZs are often attributed to compositionally distinct material associated with chemical heterogeneities along the CMB (*e.g.*, Li et al., 2017). For example, chemical interactions between the mantle and the core may generate iron-enriched material (*e.g.*, Knittle and Jeanloz, 1991), such as iron-rich post-perovskite (Mao et al., 2006), and this might account for increased ULVZ density. Alternatively, remnants from subducted material (*e.g.*, Hirose et al., 2005; Dobson and Brodholt, 2005) or remnant melt from crystallization of a basal magma ocean (Labrosse et al., 2007) have also been suggested as possible sources for ULVZ compositional heterogeneities. Further, some studies suggest that ULVZs are seen outside hotter portions of the mantle because they exist everywhere along the CMB but that they often fall below the detection capability of current methodologies (Rost and Thomas, 2010).

2.3. Possible relationship between ULVZs and LLSVPs

Seismic imaging of the Earth's interior velocity structure reveals two LLSVPs in the lower mantle, one situated beneath the Pacific and the other beneath Africa, which combined cover $\sim$30% of the CMB (Cottaar and Lekic, 2016). LLSVPs are large-scale structures, extending hundreds of kilometers above the CMB, which show δV_S of a few percent (Cottaar and Lekic, 2016; Garnero et al., 2016).

Many ULVZs have been identified along the edges of or within LLSVPs, and the abundance of ULVZs tends to decrease with distance from LLSVPs; however, it is important to note that ULVZs have also been identified far outside these areas (Li et al., 2017; Yu and Garnero, 2018). If ULVZs are purely thermal features, it is expected that they would be located along the hottest portions of the CMB, which are within LLSVPs (Hernlund and McNamara, 2015; Li et al., 2017). In contrast, ULVZs found along the edges of LLSVPs are best described by compositionally distinct material (*e.g.*, Li et al., 2017). ULVZs found far outside LLSVPs may be best explained by compositional origins, such as those described in Section 2.2.

Differentiating ULVZ origins, as well as their possible connection to LLSVPs, requires better sampling of the CMB. This study broadens CMB coverage within the southern hemisphere, mainly in the vicinity of New Zealand and along the coast of Antarctica (Fig. 1B).

3. Data and methodology

As noted in Section 1, data for the current study are provided by TAMNNET (Fig. 1A). Events with distances between 30-60° and with minimum magnitudes of 5.0 were selected, and using these criteria, the TAMNNET dataset yielded a total of 1086 events. However, from visual inspection, only 315 events displayed clear core-reflected ScP waveforms, and these events form the basis for our study. Using records from all the TAMNNET stations, the maximum ScP CMB bounce point spread for the selected, individual events ranges from $\sim$70-125 km. Across these distances, individual ScP waveforms for a given event are fairly coherent (see Supplemental Material). The average CMB bounce point locations for these events are shown in Fig. 1B.

For each event, the recorded waveforms were rotated to the P-SV-SH coordinate system so that we could focus on the longitudinal component. All data were bandpass-filtered between 0.50-1.50 Hz, which has been shown to be an effective frequency band to study P and ScP phases for CMB structure (*e.g.*, Rost et al., 2005), and using the IASP91 reference model (Kennett and Engdahl, 1991), the predicted P and ScP arrival times were determined and marked on the seismograms. The waveforms for each earthquake were initially aligned using these predicted times (Fig. 3), were normalized in amplitude, and were averaged to create linear P and ScP stacks. Next, each individual waveform was cross-correlated with the P and ScP linear stacks, respectively, to determine a cross-correlation coefficient (CCC) and delay time. The individual waveforms were then time-shifted by the correlated delay times to improve alignment of the respective signal (*i.e.*, the P or ScP). The waveforms were also weighted based on their signal-to-noise ratio (SNR) and associated CCC (see Supplemental Material). The aligned, weighted waveforms were then restacked. This process of cross-correlation, realignment, weighting, and restacking was iteratively repeated until the CCC between the newly created stack and the previous stack is greater than 0.95. This approach ensured that the waveforms were best aligned to create representative P and ScP stacks. One standard deviation was also computed for the final stacks (Fig. 3).

ScP phases travel a greater distance through the Earth's interior than direct P-waves and hence experience more attenuative energy loss; therefore, in order to compare the P and ScP stacks, the P-wave signals must be adjusted to account for any extra attenuation experienced by the ScP waves. This is accomplished by convolving the P-wave stack with a t* operator, which represents the accumulated attenuation along the ray path (*e.g.*, Futterman, 1962; Rost et al., 2005). For each event, a series of t* operators, ranging from 0.10 to 2.30, were convolved with the P-wave stack, which were then compared to the associated ScP stack. The t* which produced an attenuated P-wave response that most closely matched the as-
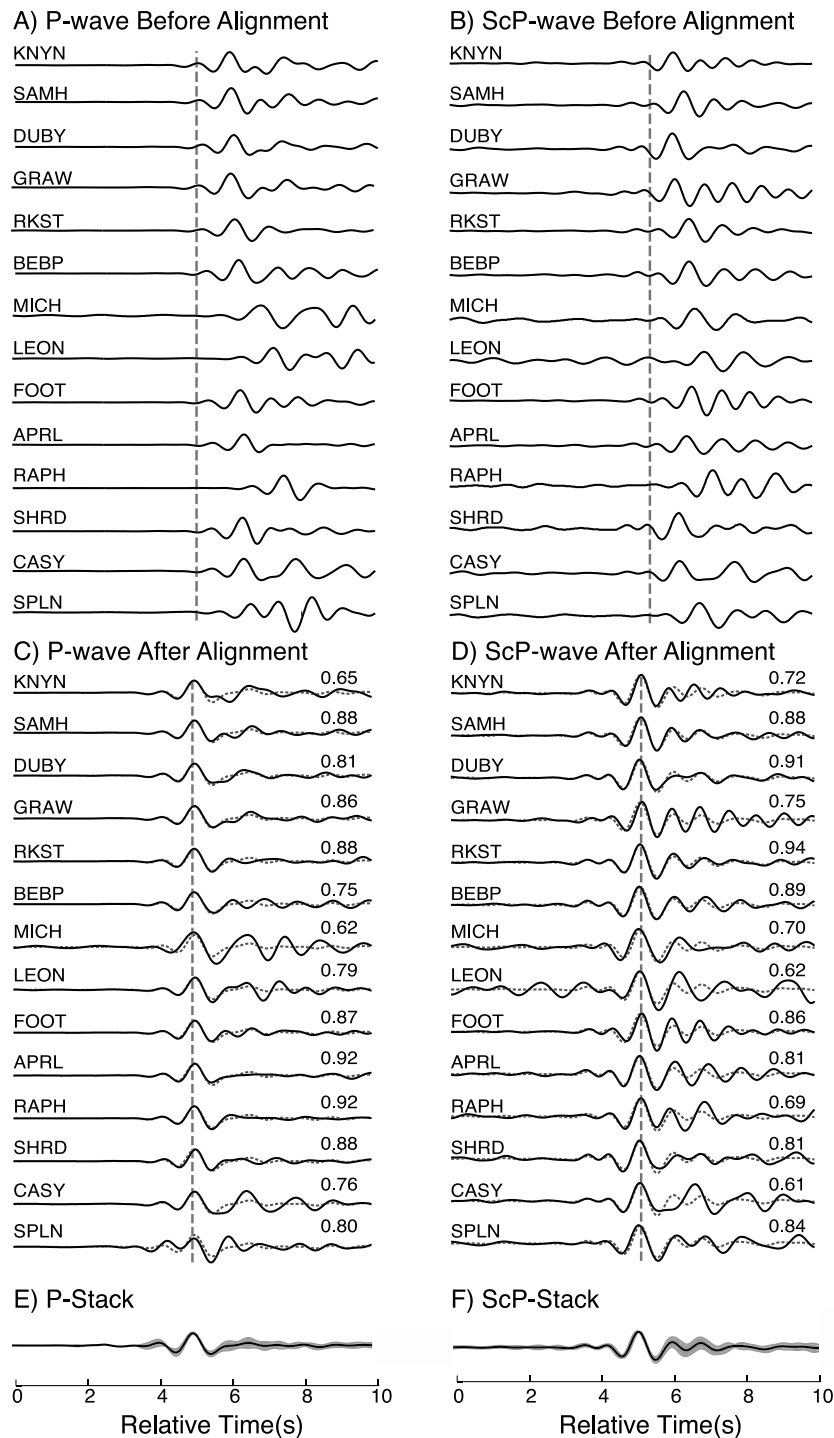
Fig. 3. Examples of P and ScP alignment and stacking. Waveforms correspond to an event that occurred on February 12, 2013 recorded by TAMNNET. The normalized P-waves (A) and ScP-waves (B) are originally aligned on their predicted arrival times from the IASP91 reference model (Kennett and Engdahl, 1991), which are marked by the dashed lines in (A) and (B). Using the correlation and weighting scheme outlined in the text, the waveforms are realigned on the waveform peak (C and D) and are stacked (E and F). In (C) and (D), the realigned waveforms (solid black traces) are shown in comparison to the respective stack (dotted gray traces). Station names are displayed on the left above each trace and CCCs are displayed on the right. The dashed vertical lines in these panels mark the peak of each arrival. In (E) and (F), one standard of deviation is also plotted around the stack (gray shaded area). Differences between the P and ScP signals, such as those illustrated here, are indicative of ULVZ structure and form the basis for our analysis.

sociated ScP signal (see Supplemental Material) was selected. The CCC between the t*-convolved P and the ScP waveforms was used to determine the best match, but all comparisons were also visually reviewed.

Each of the 315 selected events were individually processed using the steps outlined above and were then sorted into groups with A, B, or C rankings (see Supplemental Material). A-ranked events have the highest SNR, with a clear P and ScP peak and low noise over a 5-10 s window before or after the arrivals. An event was given a B ranking if it displays a clear P and ScP peak but has a higher noise level. Finally, an event was given a C ranking if it contains significant noise before the P arrival, if the P-wave

signal is too complex, or if the SNR of the ScP arrival is too low. Of the 315 analyzed events, 21 events were given an A ranking, while 50 events were given a B ranking (see Supplemental Material). These 71 events all have CMB reflection points either in the vicinity of New Zealand or beneath the Weddell Sea, and they will be the focus of further analysis to assess potential ULVZ structure. The remaining 244 C-ranked events were not examined further.

All A- and B-ranked events were also examined to ensure the polarity has not switched between the P and ScP waveforms. This can occur if the radiation pattern of the earthquake is not consistent for the direct P-wave and the initial SV wave. Since the ScP waveform begins as an SV wave, it is possible that the P and ScP waveforms may have opposite polarities. While the radiation pattern of the earthquakes can be obtained, for instance, from the Harvard centroid moment tensors (CMTs; Dziewonski et al., 1981; Ekström et al., 2012), these CMTs are derived from long-period data, and it is not uncommon for high frequency data (∼1 Hz) to display different first motions than that predicted by the CMTs. Given this, a different approach was taken to assess polarity. The ScP stack was compared to the P stack both with normal and reversed polarity (*i.e.*, the original P-stack is flipped upside down). The CCC was used as a guide to determine if the reversed polarity provides a better match between the ScP and P waves.

4. Quantifying ULVZ energy

To assess potential ULVZ-related signal in our data, the attenuated P-wave stacks were subtracted from their corresponding ScP stacks (after aligning their peaks and normalizing their amplitudes to unity) to construct remainder traces for all A- and B-ranked events, thereby highlighting the differences between them. If there is no pre- or post-cursor energy associated with ULVZ structure, the remainder trace will be relatively flat. However, if pre- or post-cursor energy is present, the remainder trace will display residual signal that is present in the ScP stack but not in the P stack (Fig. 4).

For each remainder trace, a five-second window centered on the ScP peak was defined, and the sum of the absolute amplitudes within this window defined the residual signal for that event, where high residuals are consistent with energy from ULVZ structure (Fig. 4). The window is large enough that it encompasses the dominant pre- and post-cursor ScP energy above the standard deviation uncertainty of the remainder trace for the examined events (see Supplemental Material). Outside this window, any ULVZ energy present in our data tends to fall below the uncertainty level, making it difficult to distinguish. The residual signal was normalized using the sum of the absolute amplitudes within two additional time windows: one 3.5 seconds before the residual signal and one 2.5 seconds after (Fig. 4). These two windows define the typical noise conditions in the vicinity of the ScP arrival. By dividing the residual signal by the normalizing amplitudes, we defined a normalized residual value (NRV) that establishes the strength of any ULVZ signal. That is, a NRV of approximately one indicates there is no ULVZ-related energy in our data, while a higher NRV is consistent with ULVZ energy. The NRV values are mapped to their CMB bounce point locations in Figs. 5A and 5B. When individually inspected, we could not confidently identify ULVZ pre- and/or post-cursor energy for events with NRV values less than 1.25. Of the 71 events examined, 31 had NRV values below this threshold (marked by small x's on Fig. 5), and these events were not assessed further.

5. Synthetic modeling

As shown in Fig. 5, numerous examined events in the vicinity of New Zealand and within the Weddell Sea display significant evidence for ULVZ structure. To examine these events further, 1-D
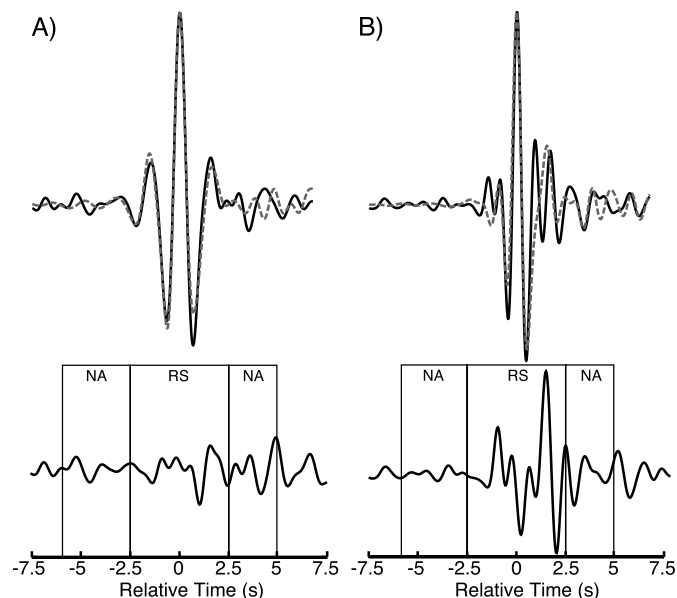

Fig. 4. Remainder traces and comparison of ULVZ energy. (top) Comparison of attenuated P-wave stacks (dashed gray traces) and ScP stacks (black traces) for events that occurred on (A) December 17 and (B) December 4, 2013, respectively. Note that these traces are very similar in (A), indicating no ULVZ energy, while the differences in (B) highlight ULVZ pre- and post-cursors. (bottom) Remainder traces for each event. Again, event (B) shows significant variability, indicative of ULVZ pre- and post-cursor energy. Boxes denote where the remainder trace is windowed to quantify the residual signal (RS) and the normalizing amplitudes (NA), respectively. The RS window encompasses the pre- and post-cursor ULVZ energy.

modeling was employed to estimate the range of ULVZ parameters (*i.e.*, thickness, δV_P, δV_S, $\delta \rho$) that fit our observed waveforms. Additionally, we wanted to investigate possible tradeoffs between ULVZ characteristics (such as between thickness and velocity reduction) and to also assess how the data are fit by a model without a ULVZ.

Given their clear P and ScP arrivals, modeling efforts were focused on A-ranked events. Further, each event had to meet certain criteria to be eligible for modeling. First, the corresponding remainder trace NRV was required to be above 1.75. Through visual inspection, it was determined that this threshold ensured significant signal associated with ULVZ structure, as defined in Section 4. Second, in some cases, variability between waveforms from different stations contributing to the stack was observed, so the corresponding standard deviation of the ScP stack was examined. For each data point in the stack, the standard deviation was determined for the normalized ScP peak, and the average was then computed. Events with average standard deviations of 0.70 or lower showed consistent ULVZ signals across all examined stations and therefore station variability did not significantly affect the ScP stack; therefore, only these events were considered. Further, we required that ScP pre- and post-cursor energy in the remainder trace must exceed an estimation of uncertainty, which we defined as one standard deviation of the remainder trace (see Supplemental Material). Together, these criteria ensure the best possible constraints for ULVZ modeling. Ultimately, only 14 events (Table 1) met all the stringent modeling criteria.

Synthetic ScP waveforms were calculated using the generalized ray method (GRM; *e.g.*, Gilbert and Helmberger, 1972), and the ScP phase, along with its SdP and SPcP pre-cursors and ScSP post-cursor, were modeled. The synthetic waveforms were computed for the range of epicentral distances covered by the data. Further, for completeness, we wanted to explore the range of ULVZ parameters found in previous investigations (see Section 2.2 and review by Yu and Garnero, 2018). More specifically, the thickness of the ULVZ
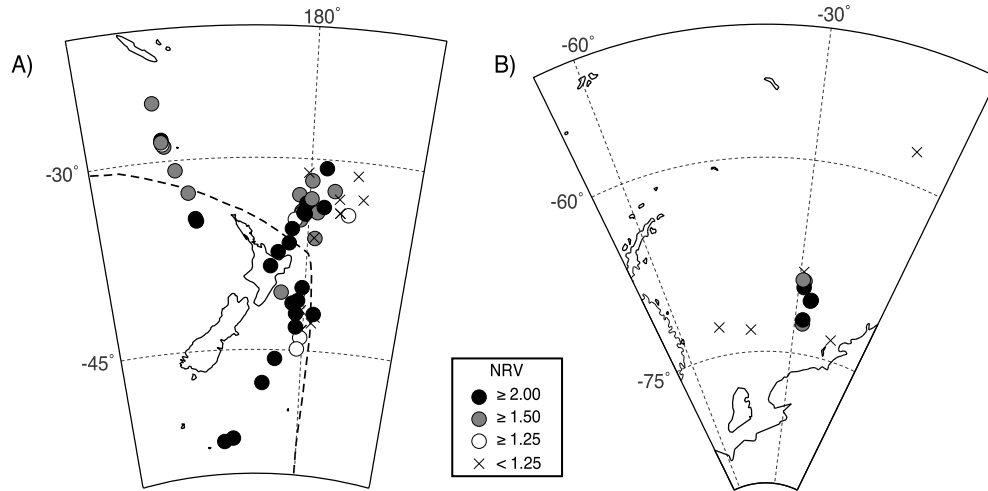
Fig. 5. ULVZ NRV maps. Remainder trace NRV for each event, plotted at the corresponding ScP CMB bounce point location in the vicinity of New Zealand (A) and the Weddell Sea (B). Darker markers indicate higher residual signal, consistent with a ULVZ. B-ranked events where the NRV was too low to confidently discern possible pre- or post-cursor signals are denoted by x's. Black dashed line in (A) highlights the LLSVP boundary as identified by the GyPSuM tomography model (Simmons et al., 2010).

Table 1
Events modeled using the 1-D Generalized Ray Method. Event dates are shown as (month/day/year). Location corresponds to the CMB bounce point locations, which are reported as either in the New Zealand (NZ) area or the Weddell Sea (WS). The NRV and average standard deviation of the remainder traces are also provided. Additional event details are provided in the Supplemental Material.

Event date	Location	NRV	Average standard deviation
11/24/12	NZ	2.00	0.54
11/29/12	NZ	1.97	0.34
02/12/13	NZ	1.85	0.61
02/16/13	NZ	2.92	0.48
04/26/13	NZ	3.89	0.29
06/15/13	NZ	2.03	0.48
07/29/13	WS	2.58	0.67
11/03/13	WS	2.09	0.60
11/23/13	NZ	2.06	0.47
12/04/13	NZ	7.78	0.22
02/01/14	WS	3.10	0.37
06/20/15	WS	2.62	0.63
06/21/15	NZ	3.81	0.37
09/07/15	NZ	4.31	0.29

was varied from 2 to 40 km in 2 km increments, and $\delta\rho$ of 0%, 10%, or 20% within the ULVZ were allowed. δV_P and δV_S ranged from 2 to 20% and 2 to 50%, respectively, in 2% increments. We also included a model without a ULVZ. Ultimately, a total of 17,141 different 1-D ULVZ models were tested.

For each event listed in Table 1, a Hanning-tapered P-wavelet was extracted from the attenuated P-wave stack using a 10 s time window centered on the maximum P-wave amplitude. The wavelet was then convolved with the synthetic spike trains generated by the GRM method to create synthetic waveforms for each examined ULVZ model. The most extreme ULVZ parameters result in pre- and post-cursors that can arrive 15-20 s before or after the main ScP peak (see Supplemental Material); therefore, to assess the full range of tested models, the synthetics were aligned with the data on the ScP peak, centered within a 40 s time window. The synthetics and observations were cross-correlated within this window, and a higher CCC (*i.e.*, closer to one) indicates a better model fit. It is worth noting that the synthetics and observations were also compared by subtracting them from one another to create a remainder trace, similar to the approach described in Section 4, and the absolute value of the remainder trace amplitudes was summed to generate a measure of misfit (*i.e.*, smaller misfit values indicate greater similarity between observations and predictions). However,

the best-fit models determined by this approach were found to be very dependent on the window length over which the signals were compared, while those determined by the cross-correlation approach were independent of window length and hence more robust (see Supplemental Material).

As summarized in Table 1, ten events in the vicinity of New Zealand and four events beneath the Weddell Sea met the modeling criteria outlined above. The ULVZ parameters associated with the top 10 best-fit synthetic models for each event (*i.e.*, those models with the 10 highest CCC values, as noted above) are summarized in Fig. 6, with the New Zealand events plotted in the top row and the Weddell Sea events plotted in the bottom row. Each subplot illustrates a comparison between different ULVZ parameters in order to assess any possible tradeoffs in the model space. We note that some models meet the best-fit criteria for more than one examined event and hence plot on top of each other in this figure. Two main observations can be made from Fig. 6. First, there is no discernible tradeoff between ULVZ parameters. This is discussed further in Section 6.2 below. Second, a majority of the best-fit models are distinguishably different from a model lacking a ULVZ (which would plot in the lower left corner of each subplot on Fig. 6), emphasizing that these events are better described by a lowermost mantle having a ULVZ. That being said, for a given New Zealand event (Fig. 6, top row), the range of the top 10 CCC values only varied by ∼0.6%, on average, from one another. Similarly, for a given Weddell Sea event (Fig. 6, bottom row), the top CCC values only varied by ∼1.0%, on average. In other words, Fig. 6 illustrates that there is a range of possible models that fit the data. This range is further illustrated in Fig. 7, where the top 5%, 10%, 20% and 40% best-fit models are denoted by progressive shading. Fig. 7 also provides a comparison between the observed waveform and the synthetic waveform from the top best-fit model for each event (determined by the CCC, as discussed above). For all modeled events, the CCC of the best-fit ULVZ model is distinguishably larger than a reference model with no ULVZ, again emphasizing that the events are better described by a ULVZ-inclusive model.

6. Discussion and interpretation

6.1. ULVZ classification

As discussed in the previous section, 14 events met our rigorous synthetic modeling criteria and showed robust evidence for ULVZ structure. That said, a conservative approach was taken to in-
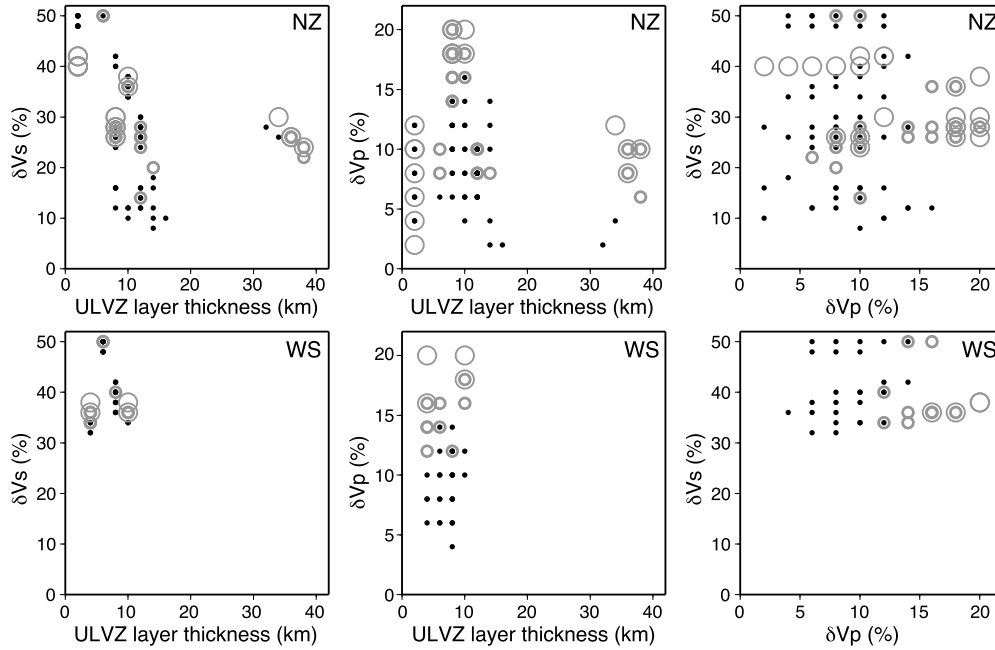
Fig. 6. ULVZ parameters for the top 10 best-fit synthetic models. Plots show (left) ULVZ thickness versus percent δV_S, (middle) ULVZ thickness versus percent δV_P, and (right) δV_P versus δV_S. In all panels, black dots correspond to synthetic models with $\delta \rho = 0\%$, gray bold circles correspond to models with $\delta \rho = 10\%$, and thin gray circles correspond to models with $\delta \rho = 20\%$. The top row corresponds to the New Zealand (NZ) events, while the bottom row corresponds to the Weddell Sea (WS) events. As noted in the text, some models meet the best-fit criteria for more than one of the examined events and hence plot on top of one another. This comparison of the different ULVZ parameters was conducted to assess any possible tradeoffs in the model space.

terpret these data, and it is quite likely that other examined events indicate the presence of ULVZ as well. For instance, if the remainder trace NRV threshold is increased to 2.00 (meaning the amount of residual signal is at least two times greater than the normalizing amplitudes), whether the events meet the standard deviation criteria or not, 16 additional events (beyond the ten in Table 1) support ULVZ evidence in the New Zealand region (Fig. 8A). That is, with this somewhat less conservative approach, the number of data suggesting ULVZ structure increases by roughly 1.5. For most of these additional events, the variability amongst waveforms at different TAMNNET stations is too high to have strong confidence in ULVZ presence. We thus conservatively mark these other sampled portions of the CMB as uncertain areas (Fig. 8A).

For the Weddell Sea region, the rigorous synthetic modeling criteria yielded four events that showed robust evidence for ULVZ. However, a NRV threshold of 2.00 (as above) does not provide any additional events with ULVZ evidence for this region (Fig. 8B). Overall, there were fewer events in this area (Figs. 1B and 5) and many were too noisy to interpret. The four modeled events are important because they show ULVZ evidence in a previously unexamined region of the CMB. These data provide the southernmost ULVZ sampling on Earth (Fig. 1B; Yu and Garnero, 2018).

### 6.2. Interpreting synthetic modeling results

The model space for the best-fit New Zealand ULVZ parameters is quite heterogeneous (Fig. 6, top row). Out of the top 10 best-fit models for all the New Zealand events, 19% have an approximate 3:1 $\delta V_S{:}\delta V_P$ ratio, consistent with partial melt (*e.g.*, Williams and Garnero, 1996; Berryman, 2000), but the remaining models suggest different velocity ratios. The δV_S and δV_P as well as the $\delta \rho$ encompassed by these models span the examined range of these three parameters. Interestingly, based on ULVZ thickness, there appears to be two distinguishable groups of top 10 best-fit models: one with ULVZ thickness between 2-16 km and the other with ULVZ thickness between 32-38 km. That being said, all of the top 10 best-fit models with the larger ULVZ thickness cor-

respond to event 02/16/2013, which is the southernmost modeled New Zealand event (Figs. 7–8A). This might indicate a thicker ULVZ in this location or a ULVZ of varying thickness.

For the Weddell Sea events, the model space is somewhat less heterogeneous (Fig. 6, bottom row). The δV_P values span the examined parameter range, which is due to the fact that the ScP pre-cursors are most sensitive to δV_P but are also lower in amplitude than the ScSP post-cursor (Brown et al., 2015). However, all of the best-fit models have δV_S greater than 32% and have ULVZ layer thicknesses between 4-10 km. $\delta \rho$ is somewhat varied, though it does appear to be higher for models with a larger δV_P. Out of all the top 10 best-fit models for the Weddell Sea events, 25% have an approximate 3:1 $\delta V_S{:}\delta V_P$ ratio, with the other models indicating different velocity ratios.

As noted previously, the range of models that fit the data are also highlighted in Fig. 7. We reiterate that the top best-fit models (red traces on Fig. 7) are purely defined by the highest CCC values, as discussed in Section 5. It is important to note that for some events, the best-fit synthetic may be only marginally better than a model with different ULVZ characteristics. Further, the best-fit model for some events is only slightly better than a model with no ULVZ, even though all the modeled events met the robust ULVZ identification criteria.

Given the range of models that fit our examined events, we cannot uniquely constrain detailed ULVZ properties; however, our findings still provide interesting insights. The New Zealand dataset is sampling a large geographic area (Fig. 8A), and the greater degree of heterogeneity that we see in these results (Figs. 6–7) may suggest that we are probing different ULVZs, which could have different thicknesses from one another. Alternatively, we may be sampling a continuous ULVZ but with variable characteristics (*i.e.*, thickness, δV_P, δV_S, $\delta \rho$). In either case, the ULVZ(s) may also be associated with complicated 3-D structure. One potential line of evidence for such 3-D structure is the fact that the additional arrivals surrounding ScP that are above the noise level are predominantly post-cursors, with pre-cursors being less common (Figs. 3, 4, and 7). This does not preclude pre-cursors obscured by noise. Previous
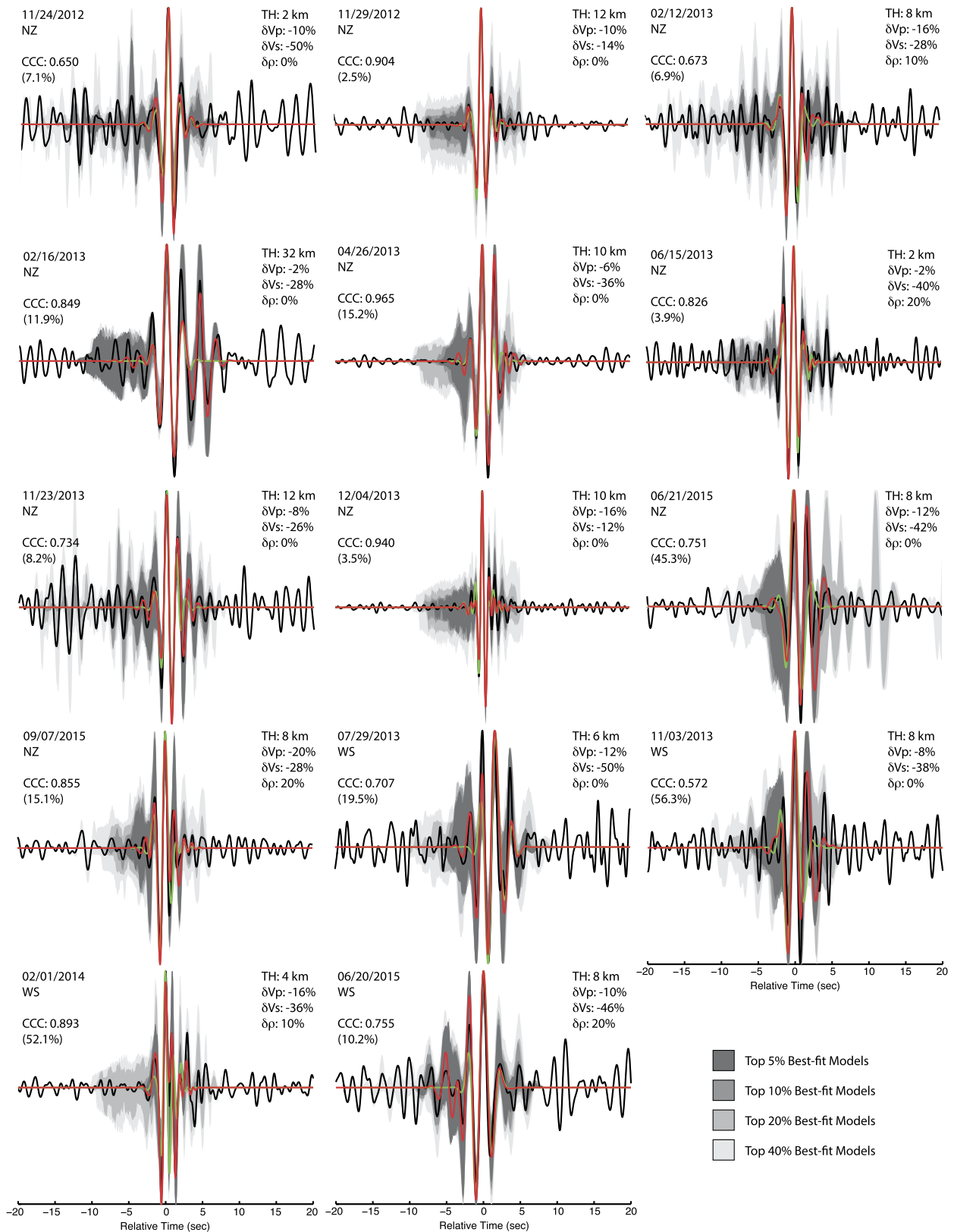
Fig. 7. Synthetic modeling. Event dates and locations are listed on the upper left (NZ: New Zealand; WS: Weddell Sea). The observed ScP stack for each event is plotted as a black trace, with its best-fit synthetic shown by a red trace. For comparison, a synthetic seismogram for a model with no ULVZ present is shown by a green trace. On the upper right, the ULVZ parameters associated with the best-fit synthetic model are listed (TH: ULVZ layer thickness; δV_P, δV_S, $\delta\rho$: V_P, V_S, and density variations). We emphasize that the best-fit synthetic is the 1-D model with the highest CCC value, as described in the text. This CCC value as well as the percent CCC improvement over a model without a ULVZ (in parenthesis) is also provided. Gray shaded areas on each panel illustrate increased misfit, with the top 5% best-fit models highlighted in dark gray and the top 10%, 20%, and 40% best-fit models denoted by progressively lighter shades of gray.
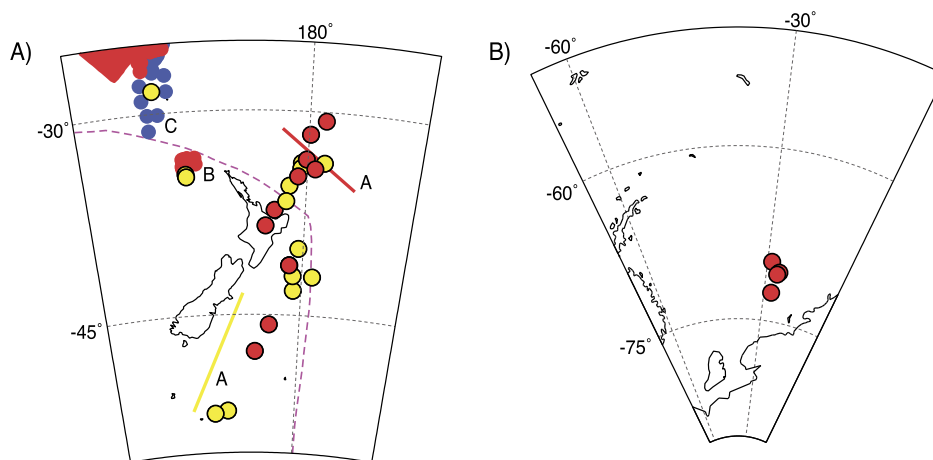
Fig. 8. ULVZ summary. Maps summarizing ULVZ evidence in (A) the vicinity of New Zealand and (B) the Weddell Sea. Contributions from the current study are shown by dots with bold black outlines, and as on Fig. 1B, red areas highlight regions where ULVZ evidence has been detected, yellow areas indicate where ULVZ evidence is uncertain, and blue areas highlight where ULVZ evidence is not identified. Letters denote previous studies. A: Thorne and Garnero (2004); B: Pachhai et al. (2015); C: Idehara et al. (2007). The purple dashed line in (A) highlights the Pacific LLSVP boundary as identified by the GyPSuM tomography model (Simmons et al., 2010).

work has noted the evidence for 3-D structure in ULVZ modeling when pre-cursors are absent but post-cursors are present (Brown et al., 2015). We note that, as discussed in Section 2.1, pre-cursors are often associated with reflections from the top of a relatively flat ULVZ (Yao and Wen, 2014). The fact that pre-cursors are less dominant in the examined dataset may suggest ULVZs with topography. Further, if the ULVZs were accurately described by 1-D structure, inherent modeling tradeoffs between ULVZ parameters, specifically between thickness and velocity reduction, would be expected (*i.e.*, a thicker ULVZ with a smaller velocity reduction is expected to tradeoff with a thinner ULVZ with a larger velocity reduction; Garnero and Helmberger, 1998). However, as noted in Section 5, such tradeoffs are not readily observed (Fig. 6).

The Weddell Sea events sample a smaller geographic region (Fig. 8B) and display fairly consistent ULVZ parameters, especially in terms of thickness and δV_S. Their larger δV_S could possibly indicate high levels of partial melt, perhaps associated with mixing of material from the mantle and the outer core; however, as noted above, only 25% of the best-fit Weddell Sea models suggest an approximate 3:1 δV_S:δV_P ratio. Further, all of the ScP CMB bounce points in this area lie within a high velocity, presumably cool region of the lower mantle (Fig. 1B). Given that the δV_S tend to cluster at the more extreme end of the examined parameter space, coupled with the wide range of δV_P (Fig. 6, bottom row), these results may also indicate complex 3-D ULVZ structure.

We emphasize that there is still strong confidence that the examined events contain ULVZ energy, given the rigorous criteria outlined in Section 5. However, the wide range of ULVZ parameters encompassed by the best-fit New Zealand models, along with the more extreme δV_S obtained for the Weddell Sea events (Figs. 6–7), strongly suggest the detected ULVZs are not simple 1-D structures. More computationally intensive 3-D modeling of ScP, combined with a larger sampling of events over smaller geographic areas (which is not available with the TAMNNET dataset), would be required to better constrain any 3-D ULVZ structure.

6.3. ULVZ interpretations

The detection of ULVZs near New Zealand provided by the current study is largely consistent with previous results, where available, and helps to bridge prior investigations (Fig. 8A). The northeast portion of the New Zealand study area coincides with a region where the global study by Thorne and Garnero (2004) found ULVZ evidence. Thorne and Garnero (2004) also examined

an area further to the south, where their ULVZ results were inconclusive. These findings are similar to those in the current study. To the northwest of New Zealand, Pachhai et al. (2015) presented evidence for a multi-layer ULVZ structure in a region where the current study finds possible but uncertain ULVZ evidence. We did not explore layered ULVZ models due to the large parameter space and the available constraints from our waveforms. In contrast, Idehara et al. (2007) did not find ULVZ evidence in the northwestern part of the study area (Fig. 8A). It is worth noting, however, that different studies using different wave path geometries may find conflicting ULVZ results. For example, further to the north of our study region, Rost et al. (2010) suggested a ULVZ within the Pacific LLSVP east of Australia in an area where Idehara et al. (2007) did not find ULVZ evidence. As previously discussed, such discrepancies may be due to 3-D ULVZ complexities.

From Fig. 8A, our results near New Zealand show ULVZs concentrated around the edge of the Pacific LLSVP. The exact location of the LLSVP boundary depends on the seismic tomography model examined (*e.g.*, Garnero et al., 2016), though Cottaar and Lekic (2016) argue that the LLSVP boundaries across all seismic tomography models are fairly similar. Regardless of which tomography model is used, the TAMNNET dataset samples both within and outside of the Pacific LLSVP and indicate ULVZ evidence along its boundary, which may be associated with chemically distinct structures moved by mantle convection currents (see Section 2.3). Li et al. (2017), for instance, illustrated this concept using geodynamical models of the lower mantle, which were run with three distinct compositions: one for the background mantle, a denser composition for a thermochemical pile (to represent LLSVPs), and a third composition to represent ULVZs. In these models, the ULVZs quickly move towards the edges of the thermochemical pile and accumulate in asymmetrical shapes, which is consistent with the ULVZs having complex 3-D structure. Our ULVZ evidence near New Zealand (Fig. 8A), combined with evidence for non-1-D structure, is consistent with this hypothesis.

As noted in Section 6.2, all of the ScP bounce points beneath the Weddell Sea lie within a high velocity, cool region of the lower mantle (Fig. 1B), far from either the Pacific or African LLSVPs. While no prior ULVZ studies have been performed in this geographic area, previous studies have found ULVZ evidence in other cool, fast regions of the lower mantle (*e.g.*, Revenaugh and Meyer, 1997; Rondenay and Fischer, 2003; Thorne and Garnero, 2004; Rost and Garnero, 2006; Xu and Koper, 2009; Jensen et al., 2013; Yao and Wen, 2014; Pachhai et al., 2015). Together, these results fur-
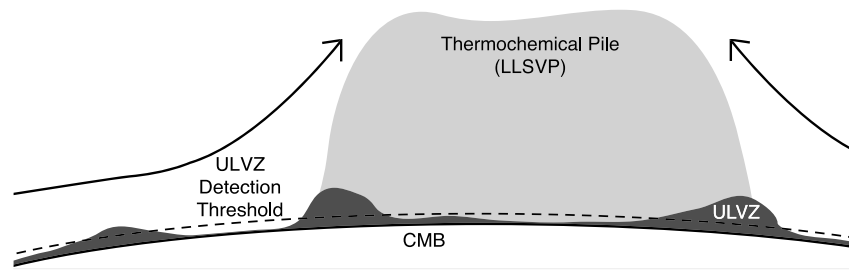
Fig. 9. Cartoon illustrating the possible relationship between ULVZs and LLSVPs. ULVZs (dark gray) may exist everywhere along the CMB, but they sometimes fall below the detection threshold (dashed line). Mantle convection currents (black arrows) sweep the ULVZs toward the edges of LLSVPs (light gray).

ther support the concept that ULVZs have a compositional origin, as opposed to a solely thermal origin, or that different mechanisms can lead to ULVZ-type velocity reductions at the CMB.

Currently, about 95% of the Antarctic Plate is surrounded by mid-ocean ridge spreading centers, with subduction only potentially occurring in the vicinity of the Shetland Plate (Bird, 2003). The northwest border of the Shetland plate is defined by the South Shetland Trench, which is a remnant of a subduction zone that once extended along the western margin of the Antarctic Peninsula (*e.g.*, Hawkes, 1981). Up until ∼3-4 Ma, the oceanic Phoenix plate subducted to the southeast beneath Antarctica at the South Shetland Trench; however, collision between the trench and a spreading ridge on the opposite side of the Phoenix plate caused subduction to slow or completely cease (*e.g.*, Klepeis and Lawver, 1996), and there is debate on whether subduction occurs along the South Shetland Trench today (*e.g.*, Alfaro et al., 2010). Whether the subducted Phoenix Plate has reached the CMB is uncertain, but the introduction of this material into the lower mantle could provide a compositional source for ULVZs, a possibility advocated by mineral physics experiments on basaltic oceanic crust (Hirose et al., 2005).

Alternatively, chemical reactions between the silicate lowermost mantle rock and the fluid iron core (Knittle and Jeanloz, 1991) may result in ULVZs everywhere along the CMB, though they may fall below seismic detection thresholds in some locations (Revenaugh and Meyer, 1997; Rost et al., 2010). Convection currents could sweep the ULVZ material into thicker, and therefore detectable, piles in certain areas, and this may be occurring beneath the Weddell Sea. Similar to the idea proposed by Li et al. (2017), ULVZ piles should eventually be swept towards areas of mantle upwelling (*e.g.*, LLSVPs), as depicted in Fig. 9. If this is the case, the ULVZs near New Zealand may be associated with chemical anomalies that have reached the LLSVP boundary, while those beneath the Weddell Sea may be currently migrating towards the African LLSVP.

7. Conclusions

This study has examined ScP waveforms recorded by the Antarctic TAMNNET deployment to further ULVZ investigations in the southern hemisphere. The CMB beneath two geographic areas is well sampled: one in the vicinity of New Zealand and the other beneath the Weddell Sea. Both study areas encompass new portions of the CMB that have not previously been investigated for ULVZ structure. Employing rigorous data quality and modeling criteria, ten ScP events with CMB bounce points near New Zealand and four events with bounce points beneath the Weddell Sea show robust evidence for pre- and post-cursor ScP energy from ULVZ structure. However, considering slightly lower quality data yields an additional 16 events sampling the CMB near New Zealand that show plausible evidence for ULVZs. The TAMNNET dataset is dominated by ScP waves mostly having post-cursor energy, and combined with a broad parameter range for permissible ULVZ solution models, may point to complex 3-D ULVZ structure.

While ULVZ parameters (*i.e.*, thickness, δV_P, δV_S, $\delta\rho$) cannot be uniquely determined with this dataset, ultra-low velocities are clearly required, and standard reference models cannot reproduce the observed waveforms. The sampled locations requiring ULVZs are consistent with a chemically distinct origin, as they are found both along the edges of and far outside of LLSVPs (*i.e.*, the putative hottest lowermost mantle regions). A number of sources might relate to such chemically distinct origins, including melt residue from fractional crystalization of a basal magma ocean, chemical reactions along the CMB, such as iron-rich post-perovskite, or subducted material. Mantle convection currents may sweep compositionally distinct ULVZs toward the boundaries of LLSVPs, such as the region near New Zealand where ULVZs have been identified. ULVZs observed beneath the Weddell Sea may be currently migrating towards the African LLSVP.

Declaration of competing interest

The authors declare that they have no known competing financial interests or personal relationships that could have appeared to influence the work reported in this paper.

Appendix A. Supplementary material

Supplementary material related to this article can be found online at https://doi.org/10.1016/j.epsl.2020.116142.

References

Alfaro, P., Lopez-Martinez, J., Maestro, A., Galindo-Zaldivar, J., Duran-Valsero, J.J., Cuchi, J.A., 2010. Recent tectonic and morphostructural evolution of Byers Peninsula (Antarctica): insight into the development of the South Shetland Islands and Bransfield Basin. J. Iber. Geol. 36 (1), 21–38.

Avants, M., Lay, T., Garnero, E.J., 2006. A new probe of ULVZ S-wave velocity structure: array stacking of ScS waveforms. Geophys. Res. Lett. 330 (7). https://doi.org/10.1029/2005GL024989.

Berryman, J.G., 2000. Seismic velocity decrement ratios for regions of partial melt in the lower mantle. Geophys. Res. Lett. 27, 421–424. https://doi.org/10.1029/1999GL008402.

Bird, P., 2003. An updated digital model of plate boundaries. Geochem. Geophys. Geosyst. 4 (3), 1027. https://doi.org/10.1029/2001GC000252.

Brown, S.P., Thorne, M.S., Miyagi, L., Rost, S., 2015. A compositional origin to ultralow-velocity zones. Geophys. Res. Lett. 42, 1039–1045. https://doi.org/10.1002/2014GL062097.

Cottaar, S., Romanowicz, B., 2012. An unusually large ULVZ at the base of the mantle near Hawaii. Earth Planet. Sci. Lett. 355–356, 213–222. https://doi.org/10.1016/j.epsl.2012.09.005.

Cottaar, S., Lekic, V., 2016. Morphology of seismically slow lower mantle structures. Geophys. J. Int. 207, 1122–1136. https://doi.org/10.1093/gji/ggw324.

Dobson, D.P., Brodholt, J.P., 2005. Subducted banded iron formations as a source of ultra-low velocity zones at the core-mantle boundary. Nature 434, 371–374. https://doi.org/10.1038/nature03430.

Dziewonski, A.M., Chou, T.-A., Woodhouse, J.H., 1981. Determination of earthquake source parameters from waveform data for studies of global and regional seismicity. J. Geophys. Res. 86, 2825–2852. https://doi.org/10.1029/JB086iB04p02825.

Ekström, G., Nettles, M., Dziewonski, A.M., 2012. The global CMT project 2004-2010: centroid-moment tensors for 13,017 earthquakes. Phys. Earth Planet. Inter. 200–201, 1–9. https://doi.org/10.1016/j.pepi.2012.04.002.

Fretwell, P., et al., 2013. Bedmap2: improved ice bed, surface and thickness datasets for Antarctica. Cryosphere 7, 375–393. https://doi.org/10.5194/tc-7-375-2013.

Frost, D., Rost, S., Selby, N.D., Stuart, G.W., 2013. Detection of a tall ridge at the core- mantle boundary from scattered PKP energy. Geophys. J. Int. 195, 558–574. https://doi.org/10.1093/gji/ggt242.

Futterman, W.I., 1962. Dispersive body waves. J. Geophys. Res. 67, 5279–5291. https://doi.org/10.1029/JZ067i013p05279.

Garnero, E.J., Helmberger, D.V., 1998. Further structural constraints and uncertainties of a thin laterally varying ultralow-velocity layer at the base of the mantle. J. Geophys. Res. 103 (B6), 12495–12509. https://doi.org/10.1029/98JB00700.

Garnero, E.J., Vidale, J.E., 1999. ScP: a probe of ultralow velocity zones at the base of the mantle. Geophys. Res. Lett. 26 (3), 377–380. https://doi.org/10.1029/1998GL900319.

Garnero, E.J., 2000. Heterogeneity of the lowermost mantle. Annu. Rev. Earth Planet. Sci. 28, 509–537. https://doi.org/10.1126/science.1148028.

Garnero, E.J., McNamara, A.K., Shim, S., 2016. Continent-sized anomalous zones with low seismic velocity at the base of Earth's mantle. Nat. Geosci. 9, 481–489. https://doi.org/10.1038/ngeo2733.

Gilbert, F., Helmberger, D.V., 1972. Generalized ray theory for a layered sphere. Geophys. J. R. Astron. Soc. 27, 57–80. https://doi.org/10.1111/j.1365-246X.1972.tb02347.x.

Hansen, S.E., Reusch, A., Parker, T., Bloomquist, D., Carpenter, P., Graw, J.H., Brenn, G.R., 2015. The Transantarctic Mountains Northern Network (TAMNNET): deployment and performance of a seismic array in Antarctica. Seismol. Res. Lett. 86, 1636–1644. https://doi.org/10.1785/0220150117.

Havens, E., Revenaugh, J., 2001. A broadband seismic study of the lowermost mantle beneath Mexico: constraints on ultralow velocity zone elasticity and density. J. Geophys. Res., Solid Earth 106 (B12), 30809–30820. https://doi.org/10.1029/2000JB000072.

Hawkes, D.D., 1981. Tectonic segmentation of the northern Antarctic Peninsula. Geology 9 (5), 220–224. https://doi.org/10.1130/0091-7613(1981)9<220:TSOTNA>2.0.CO;2.

Hernlund, J.W., McNamara, A.K., 2015. The core-mantle boundary region. Treatise Geophys. 7, 461–519. https://doi.org/10.1016/B978-0-444-53802-4.00136-6.

Hirose, K., Takafuji, N., Sata, N., Ohishi, Y., 2005. Phase transition and density of subducted MORB crust in the lower mantle. Earth Planet. Sci. Lett. 237, 239–251. https://doi.org/10.1016/j.epsl.2005.06.035.

Idehara, K., Yamada, A., Zhao, D., 2007. Seismological constraints on the ultralow velocity zones in the lowermost mantle from core-reflected waves. Phys. Earth Planet. Inter. 165 (1–2), 25–46. https://doi.org/10.1016/j.pepi.2007.07.005.

Jensen, K.J., Thorne, M.S., Rost, S., 2013. SPdKS analysis of ultralow-velocity zones beneath the western Pacific. Geophys. Res. Lett. 40, 4574–4578. https://doi.org/10.1002/grl.50877.

Kennett, B.L.N., Engdahl, E.R., 1991. Travel times for global earthquake location and phase association. Geophys. J. Int. 105, 429–465. https://doi.org/10.17611/DP/9991809.

Klepeis, K.A., Lawver, L.A., 1996. Tectonics of the Antarctica-Scotia plate boundary near Elephant and Clarence Islands, West Antarctica. J. Geophys. Res. 101, 20211–20231. https://doi.org/10.1029/96JB01510.

Knittle, E., Jeanloz, R., 1991. Earth's core–mantle boundary − results of experiments at high-pressures and temperatures. Science 251 (5000), 1438–1443. https://doi.org/10.1126/science.251.5000.1438.

Labrosse, S., Hernlund, J.W., Coltice, N., 2007. A crystallizing dense magma ocean at the base of the Earth's mantle. Nature 450 (7171), 866–869. https://doi.org/10.1038/nature06355.

Li, M., McNamara, A.K., Garnero, E.J., Yu, S., 2017. Nat. Commun. 8, 177. https://doi.org/10.1038/s41467-017-00219-x.

Mao, W.L., Mao, H.K., Sturhahn, W., Zhao, J.Y., Prakapenka, V.B., Meng, Y., Shu, J.F., Fei, Y.W., Hemley, R.J., 2006. Iron-rich post-perovskite and the origin of ultralow-velocity zones. Science 312 (5773), 564–565. https://doi.org/10.1126/science.1123442.

Pachhai, S., Dettmer, J., Tkalčić, H., 2015. Ultra-low velocity zones beneath the Philippine and Tasman Seas revealed by a transdimensional Bayesian waveform inversion. Geophys. J. Int. 203 (2), 1302–1318. https://doi.org/10.1093/gji/ggv368.

Reasoner, C., Revenaugh, J., 2000. ScP constraints on ultralow-velocity zone density and gradient thickness beneath the Pacific. J. Geophys. Res., Solid Earth 105 (B12), 28173–28182. https://doi.org/10.1029/2000JB900331.

Revenaugh, J., Meyer, R., 1997. Seismic evidence of partial melt within a possibly ubiquitous low-velocity layer at the base of the mantle. Science 277 (5326), 670–673. https://doi.org/10.1126/science.277.5326.670.

Rondenay, S., Fischer, K.M., 2003. Constraints on localized core-mantle boundary structure from multichannel, broadband SKS coda analysis. J. Geophys. Res., Solid Earth 108 (B11), 2537. https://doi.org/10.1029/2003JB002518.

Rost, S., Revenaugh, J., 2003. Small-scale ultralow-velocity zone structure imaged by ScP. J. Geophys. Res., Solid Earth 108 (B1). https://doi.org/10.1029/2001JB001627, 2056.

Rost, S., Garnero, E.J., Williams, Q., Manga, M., 2005. Seismological constraints on a possible plume root at the core-mantle boundary. Nature 435 (7042), 666–669. https://doi.org/10.1038/nature03620.

Rost, S., Garnero, E.J., 2006. Detection of an ultralow velocity zone at the core-mantle boundary using diffracted PKKPab waves. J. Geophys. Res., Solid Earth 111, B07309. https://doi.org/10.1029/2005JB003850.

Rost, S., Garnero, E.J., Williams, Q., 2006. Fine-scale ultralow-velocity zone structure from high-frequency seismic array data. J. Geophys. Res., Solid Earth 111, B09310. https://doi.org/10.1029/2005JB004088.

Rost, S., Garnero, E.J., Stefan, W., 2010. Thin and intermittent ultralow-velocity zones. J. Geophys. Res., Solid Earth 115, B06312. https://doi.org/10.1029/2009JB006981.

Rost, S., Thomas, C., 2010. High resolution CMB imaging from migration of short-period core reflected phases. Phys. Earth Planet. Inter. 183, 143–150. https://doi.org/10.1016/j.pepi.2010.04.005.

Simmons, N.A., Forte, A.M., Boschi, L., Grand, S.P., 2010. GyPSuM: a joint tomographic model of mantle density and seismic wave speeds. J. Geophys. Res., Solid Earth 115, B12310. https://doi.org/10.1029/2010JB007631.

Thorne, M.S., Garnero, E.J., 2004. Inferences on ultralow-velocity zone structure from a global analysis of SPdKS waves. J. Geophys. Res., Solid Earth 109, B08301. https://doi.org/10.1029/2004JB003010.

Thorne, M.S., Garnero, E.J., Jahnke, G., Igel, H., McNamara, A.K., 2013. Mega ultra low velocity zone and mantle flow. Earth Planet. Sci. Lett. 364, 59–67. https://doi.org/10.1016/j.epsl.2012.12.034.

Wessel, P., Smith, W.H.F., 1995. New version of the Generic Mapping Tools released. Eos Trans. AGU 76 (33), 329. https://doi.org/10.1029/95EO00198.

Williams, Q., Garnero, E.J., 1996. Seismic evidence for partial melt at the base of Earth's mantle. Science 273 (5281), 1528–1530. https://doi.org/10.1126/science.273.5281.1528.

Williams, Q., Revenaugh, J., Garnero, E.J., 1998. A correlation between ultra-low basal velocities in the mantle and hot spots. Science 281 (5376), 546–549. https://doi.org/10.1126/science.281.5376.546.

Xu, Y., Koper, K.D., 2009. Detection of a ULVZ at the base of the mantle beneath the northwest Pacific. Geophys. Res. Lett. 36, L14612. https://doi.org/10.1029/2009GL039387.

Yao, J., Wen, L., 2014. Seismic structure and ultra-low velocity zones at the base of the Earth's mantle beneath Southeast Asia. Phys. Earth Planet. Inter. 233, 103–111. https://doi.org/10.1016/j.pepi.2014.05.009.

Yu, S., Garnero, E.J., 2018. Ultralow velocity zone locations: a global assessment. Geochem. Geophys. Geosyst. 19, 396–414. https://doi.org/10.1002/2017GC007281.